

Analog quantum simulation of the Lipkin-Meshkov-Glick model in a transmon qudit

Elizabeth Champion,^{1,2} Annie Schwartz,^{1,2} Muhammad A. Ijaz,^{1,2} Xiaohui Xu,^{1,2} Steve Campbell,^{3,4} Gabriel T. Landi,^{1,2} and Machiel S. Blok^{1,2,*}

¹*Department of Physics and Astronomy, University of Rochester, Rochester, New York 14627, USA*

²*University of Rochester Center for Coherence and Quantum Science, Rochester, New York 14627, USA*

³*School of Physics, University College Dublin, Belfield, Dublin 4, Ireland*

⁴*Centre for Quantum Engineering, Science, and Technology, University College Dublin, Dublin 4, Ireland*

(Dated: December 8, 2025)

The simulation of large-scale quantum systems is one of the most sought-after applications of quantum computers. Of particular interest for near-term demonstrations of quantum computational advantage are analog quantum simulations, which employ analog controls instead of digitized gates. Most analog quantum simulations to date, however, have been performed using qubit-based processors, despite the fact that many physical systems are more naturally represented in terms of qudits (i.e., d -level systems). Motivated by this, we present an experimental realization of the Lipkin-Meshkov-Glick (LMG) model using an analog simulator based on a single superconducting transmon qudit with up to $d = 9$ levels. This is accomplished by moving to a rotated frame in which evolution under any time-dependent local field and one-axis twisting can be realized by the application of multiple simultaneous drives. Combining this analog drive scheme with universal control and single-shot readout of the qudit state, we provide a detailed study of five finite-size precursors of quantum criticality in the LMG model: dynamical phase transitions, closing of the energy gap, Kibble-Zurek-like dynamics, statistics of the order parameter, and excited-state phase transitions. For each experiment we devise a protocol for extracting the relevant properties which does not require any prior knowledge of the system eigenstates, and can therefore be readily extended to higher dimensions or more complicated models. Our results cement high-dimensional transmon qudits as an exciting path towards simulating many-body physics.

Simulating the dynamics of large quantum systems is a promising application for quantum computation [1, 2]. Recent qubit-based experiments explored a range of interesting dynamical quantum phenomena including topological order in strongly interacting fermions [3], string breaking in lattice gauge theories [4], and quantum criticality in spin lattices [5]. Ultimately, the goal of quantum simulation is to emulate classically intractable problems with physical relevance. However, not all physically relevant systems are easily emulated using qubits. Many physical systems of interest have higher-dimensional local Hilbert spaces, and encoding a high-dimensional quantum system into multiple qubits requires engineering complex (non-local) multi-body interactions, introducing significant overhead. These challenges suggest that exciting new opportunities may emerge from exploring quantum evolution in qudit-based simulators [6–14], in which two-level qubits are replaced by d -level quantum systems.

An ideal subject of study for qudit-based simulators is the Lipkin-Meshkov-Glick (LMG) model [15]. This is a widely used model in many-body physics, whose large-spin Hamiltonian is naturally encoded into a qudit. The LMG model hosts a rich variety of quantum critical phenomena [16–18] owing to a competition between the local field (J_z) and one-axis-twisting (OAT, J_x^2) terms. Despite rapid progress in the development of qudit architectures for quantum information processing [19–28] and

quantum simulation [11, 29–33], a qudit simulator with tunable local fields and OAT has thus far not been realized. A static qudit-OAT term can arise naturally in nuclear spins through the quadrupole splitting [21, 22] or can be mapped to a Kerr nonlinearity in transmons [34]. For these systems the OAT term provides the nonlinearity that enables universal control, but it is challenging to tune the term in-situ because resonant control fields do not obey the parity symmetry of the OAT term. A realization of programmable OAT in qudits would be a powerful addition to the simulator toolbox for studying dynamical qudit phenomena [35].

In this work we engineer local fields and one-axis twisting in a high- E_J/E_C superconducting transmon qudit with up to $d = 9$ levels [28] to study quantum criticality in the LMG model. Analog evolution under the LMG Hamiltonian is realized in a rotating frame by applying simultaneous drive tones close to each qudit transition [34], where the detunings and amplitudes of the drives are independently varied to parametrize the local field and OAT. We furthermore develop an adiabatic protocol that facilitates the preparation of LMG eigenstates and their superpositions without requiring any prior knowledge of the Hamiltonian’s eigenstates – a crucial condition for future quantum simulators. With these tools, we experimentally investigate a total of five aspects of the LMG criticality: (1) dynamical phase transitions, (2) closing of the energy gap, (3) Kibble-Zurek-like dynamics, (4) statistics of the order parameter, and (5) excited-state phase transitions. Our experiments involve spin sizes below the scaling

* machielblok@rochester.edu

region, and therefore shed light on the finite-size precursors of these phase transitions, and how they can be probed experimentally in a system with universal quantum control. In conjunction with recent work on transmon qudit entangling gates [24–26], our results lay the groundwork for quantum simulation of complex qudit-based Hamiltonians with future applications in particle physics [6–12], quantum chemistry [13], and condensed matter [14].

The LMG model was first introduced as a testbed for many-body approximation methods in the context of nuclear physics because it has exact analytical solutions in some cases, yet features interesting quantum phenomena [15]. The model can be formulated as N degenerate, all-to-all interacting spin-1/2 particles subject to an external field, with Hilbert space dimension 2^N . However, the structure of the model permits a collective spin representation in which the highest-spin sector has size $j = N/2$ (for simplicity, in this work we consider integer j). In this picture the Hamiltonian is given by

$$H/\Omega = -hJ_z - \frac{\gamma_x}{2j}J_x^2 - \frac{\gamma_y}{2j}J_y^2, \quad (1)$$

where h is the field strength, γ_x and γ_y describe the twisting terms (corresponding to interaction terms in the many-body model), and $\hbar = 1$. We take the parameters h , γ_x , and γ_y to be dimensionless, and fix the simulation energy scale to $\Omega/(2\pi) = 1.910$ MHz unless stated otherwise. Here we focus on the one-axis twisting case, where $\gamma_y = 0$,

$$H_{\text{LMG}}/\Omega = -hJ_z - \frac{\gamma_x}{2j}J_x^2, \quad (2)$$

although we note that the inclusion of the J_y^2 term (leading to two-axis twisting) is straightforward in our experimental setup. We denote J_z eigenstates by $|j, m\rangle$ for $-j \leq m \leq j$ such that $J_z|j, m\rangle = m|j, m\rangle$. The eigenstates of J_x are denoted by $|j, m\rangle_x$ such that $J_x|j, m\rangle_x = m|j, m\rangle_x$.

The Hamiltonian (2) is invariant under the \mathbb{Z}_2 transformation $(J_x, J_y, J_z) \rightarrow (-J_x, -J_y, J_z)$, i.e., a rotation by π about the z axis. We define a parity operator $\Pi = \exp[i\pi(J_z - j)]$, which has degenerate eigenvalues ± 1 corresponding to even and odd parities respectively. The additional factor of $e^{-i\pi j}$ ensures that the ground state is always in the even-parity sector. Because H_{LMG} commutes with Π , they share an eigenbasis. In the limit where $h/\gamma_x \gg 1$ the definite-parity eigenstates are the J_z eigenstates, while for $h/\gamma_x \ll 1$ they are given by $|j, m\rangle_{\pm} = \frac{1}{\sqrt{2}}(|j, m\rangle_x \pm |j, -m\rangle_x)$ when $m \neq 0$, and $|j, 0\rangle_{+} = |j, 0\rangle_x$; see the Supplemental Material for details.

We can develop intuition for the LMG model through a semiclassical analysis [16, 18] where $J_{x,y,z}$ are imagined as the components of a vector on a sphere of radius j ,

$$\mathbf{J} = j(\sin \theta \cos \phi, \sin \theta \sin \phi, \cos \theta), \quad (3)$$

with classical energy surface

$$\frac{E(\theta, \phi)}{j} = -h \cos \theta - \frac{\gamma_x}{2} \sin^2 \theta \cos^2 \phi. \quad (4)$$

For $h/\gamma_x \geq 1$ this has a single minimum at $\theta_0 = 0$, and this region is henceforth referred to as the normal phase. For $h/\gamma_x < 1$ OAT dominates, leading to two degenerate minima located at $\theta_0 = \pm \arccos(h/\gamma_x)$ and $\phi = 0$, and we call this region the symmetry-broken phase (see the Supplemental Material for details). The energy surfaces are shown in Figure 1e, along with Husimi Q functions for the $j = 4$ ground states.

In this work we experimentally investigate the properties of the LMG model using a fixed-frequency transmon qudit of dimension $d = 2j + 1$. All experiments were carried out using the transmon labeled Q_5 in Ref. [28], which was designed to have $E_J/E_C \approx 300$ [36, 37]. This ensures that a large number of states are confined in the cosine potential, and strongly suppresses charge dispersion for all states used in this work (Figure 1a). By selectively driving individual transitions, we can prepare arbitrary qudit states and perform arbitrary unitary rotations with high fidelity [24, 27, 28, 34]. Meanwhile, a dispersively coupled readout resonator facilitates single-shot readout of the full qudit state (Figure 1b). We provide device parameters and coherence time measurements in the Supplemental Material, and refer the reader to Ref. [28] for a detailed discussion of the device properties and the multi-tone readout protocol.

The LMG Hamiltonian is simulated by applying simultaneous drives with frequencies near the transmon's single-photon transitions. Denoting the transmon eigenstates by $|n\rangle$ for $0 \leq n < d$, we show (see Methods) that moving to a rotating frame that is detuned from the bare transmon frame and taking the rotating wave approximation (RWA) yields a Hamiltonian of the form

$$H(t) = \sum_{n=0}^{d-1} \Delta_n(t) |n\rangle \langle n| + \sum_{n=1}^{d-1} \left(\Omega_n(t) |n-1\rangle \langle n| + \text{h.c.} \right), \quad (5)$$

where $\Omega_n(t)$, $\Delta_n(t)$ are the amplitudes and detunings of the drives that appear on the first off-diagonal and diagonal, respectively (Figure 1d, left). Meanwhile, writing the LMG Hamiltonian in the J_z basis, we find that it contains nonzero matrix elements only on the diagonal and second off-diagonals, as depicted in the right panel of Figure 1d. Importantly, however, we are free to encode the Hilbert space of the emulated spin into the transmon Hilbert space in whichever manner is most convenient. As shown in Figure 1c, we encode the even-parity J_z eigenstates in the lowest $j + 1$ transmon eigenstates, and the odd-parity J_z eigenstates in the remaining j transmon states. This relabeling of the Hilbert space has the effect of moving the second-off-diagonal (OAT) elements onto the first off-diagonals (Figure 1d, left), thereby allowing for the direct analog simulation of the LMG model. The drive amplitudes, detunings,

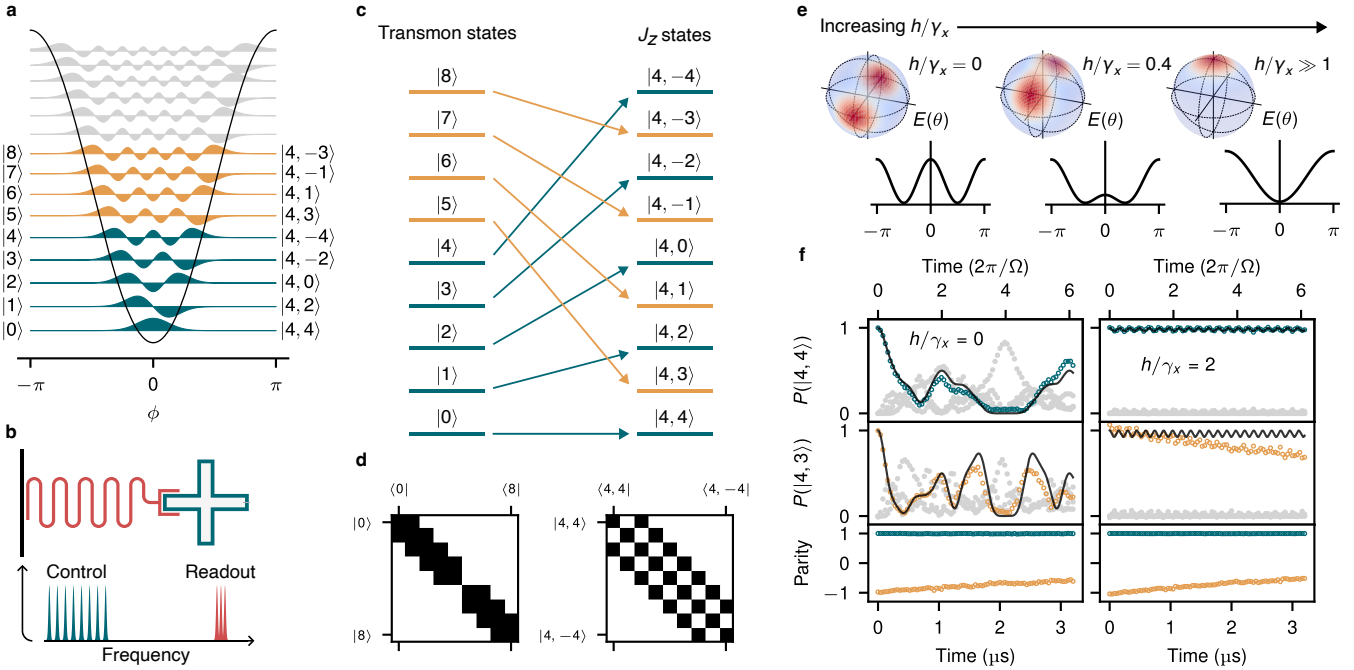


FIG. 1. Analog quantum simulation of the LMG model. **a**, High- E_J/E_C transmon potential well and eigenstate wavefunctions. The state labels on the left indicate the physical transmon states, while those on the right indicate the encoded spin states. **b**, Diagram of the transmon and resonator (top) and the drive spectrum used for control and readout (bottom, not to scale). Multiple simultaneous drive tones are used to simulate the LMG Hamiltonian in a rotating frame, and three simultaneous readout tones enable single-shot measurement of the qudit state. **c**, Diagram of the state labeling scheme. The even-parity spin states are encoded into the lowest $j+1$ levels of the transmon, while the odd-parity spin states are encoded into the remaining j levels. **d**, Nonzero matrix elements of the LMG Hamiltonian in the transmon basis (left) and the J_z basis (right). In the J_z basis the Hamiltonian has nonzero elements on the diagonal and second off-diagonals, while in the transmon basis, it has elements on the diagonal and first off-diagonals. **e**, Symmetry-broken and normal phases of the LMG model. We show the Husimi Q functions of the LMG ground states for $j=4$ with $h/\gamma_x=0$ (top left), $h/\gamma_x=0.4$ (top middle), and $h/\gamma_x \gg 1$ (top right). The corresponding semiclassical energy surfaces are shown in the bottom row. **f**, Experimentally measured evolution of the J_z eigenstates $|4, 4\rangle$ (top) and $|4, 3\rangle$ (middle) under the $j=4$ LMG Hamiltonian with $h/\gamma_x=0$ (left) and $h/\gamma_x=2$ (right). Colored points give the measured populations in the initial states, solid lines indicate the theoretical evolution, and gray points give the other measured populations within the same-parity subspaces. The bottom panels show the expectation value of the parity operator in each case, showing that parity is preserved up to T_1 decay from the odd subspace into the even subspace.

and phases are determined by computing H_{LMG} in this relabeled basis and comparing to Eq. 5.

We now present the results of several experiments which probe the finite-size precursors of quantum criticality in the LMG model. We give a detailed explanation of the protocol for each experiment in the Methods section.

Dynamical phase transition

We demonstrate the time evolution of the system under the LMG Hamiltonian for $j=4$ in Figure 1f, where in the top row we begin in the state $|4, 4\rangle$ and in the middle row we begin in $|4, 3\rangle$. The left column corresponds to evolution in the symmetry-broken phase ($h=0$) and the right column in the normal phase ($h=2$); in both cases we set $\gamma_x=1$. The colored points represent the Loschmidt Echo (return probability) and the gray dots

are the occupation probabilities for the other J_z eigenstates of the same parity. When $h=0$ the initial states are not close to eigenstates of the Hamiltonian, so we observe that the system quickly evolves away from its initial state, in agreement with the theoretical predictions (solid lines). The system undergoes coherent oscillations between J_z eigenstates (Figure 1f, left) and rapidly evolves to a state nearly orthogonal to its initial state, representing a finite-size precursor of the dynamical phase transition [38–43] and the so-called orthogonality catastrophe [44, 45]. This behavior is also closely related to the LMG model’s excited-state quantum phase transition, discussed further below. Meanwhile, when $h=2$ (Figure 1f, right column) the LMG eigenstates are close to those of J_z , causing the return probabilities to remain close to 1. In the bottom row of Figure 1f we plot the expectation value of the parity operator for each case, computed from the measured populations. The parity should ideally be $\langle \Pi \rangle = \pm 1$ for all times, because we begin in

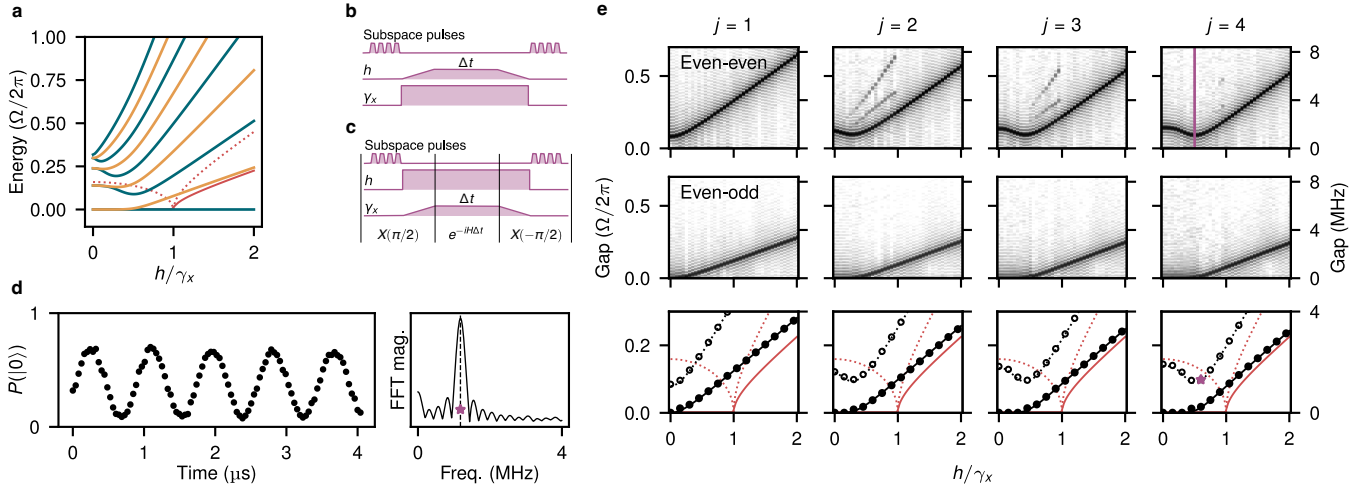


FIG. 2. Adiabatic protocol and gap measurement. **a**, Energy spectrum of the LMG model with $j = 4$ as a function of h/γ_x . The even-parity states are shown in blue, and odd-parity in yellow. In this experiment we focus on the lowest even-odd and even-even energy gaps. These gaps in the thermodynamic limit are shown in red. **b**, Gap measurement protocol for $h/\gamma_x < 1$. **c**, Gap measurement protocol for $h/\gamma_x > 1$. Both protocols implement Ramsey-like experiments in which we adiabatically prepare equal superpositions of LMG eigenstates, evolve under the LMG Hamiltonian, and project the resulting state onto the initial state. **d**, Time trace (left) and Fourier transform (right) for a single gap experiment with $j = 4$ and $h/\gamma_x = 0.6$. This corresponds to the purple line in the top right panel of **e**, and the peak of the Fourier transform gives the energy indicated by the purple star in the bottom right panel of **e**. **e**, Experimental results for the even-even (top) and even-odd (middle) gaps across a range of h/γ_x values. The plots are obtained by computing the Fourier transform of each Ramsey signal as shown in **d** and plotting the logarithm of its magnitude in grayscale. We see strong peaks corresponding to the gap. In the bottom row we extract the frequencies of these peaks (open circles for even-even, filled circles for even-odd) and plot them on top of the theoretically expected values (dashed black line for even-even, solid black line for even-odd). We also show the corresponding gaps in the thermodynamic limit, $j \rightarrow \infty$, in red.

states of definite parity. For the even-parity case the parity remains essentially unchanged during the dynamics, while for odd-parity case (beginning in $|4, 3\rangle$) we observe that the parity slowly evolves away from -1 , owing to gradual T_1 decay of the transmon from the odd-parity subspace into the even-parity subspace. This experiment thus showcases the ability of our analog simulator to preserve the underlying symmetries of the model.

Closing of the ground-state gap

In our next experiment we measure the LMG model's energy spectrum, focusing on gaps between low-energy states within the same-parity subspace as well as between subspaces. We show the spectrum of the system for $j = 4$ as a function of h/γ_x in Figure 2a. We note that, in the thermodynamic limit, the closing of the energy gaps at $h/\gamma_x = 1$ (see, e.g., the red curves in Figure 2a) is a signature of the transition between the symmetric and symmetry-broken phases. Here we measure the energy gaps between the ground state (even-parity) and the first and second excited states, which have odd and even parities, respectively. We denote these, respectively, by $|0_{\text{LMG}}\rangle$, $|1_{\text{LMG}}\rangle$, and $|2_{\text{LMG}}\rangle$. We measure the energy gaps $E_{\text{even-odd}} = E_{|1_{\text{LMG}}\rangle} - E_{|0_{\text{LMG}}\rangle}$ and $E_{\text{even-even}} = E_{|2_{\text{LMG}}\rangle} - E_{|0_{\text{LMG}}\rangle}$ by performing Ramsey

style experiments in which we prepare equal superpositions of the states of interest and evolve under the LMG Hamiltonian for a variable time Δt , imparting a phase difference $-E\Delta t$ between the eigenstates. Projecting the final state onto the initial superposition results in an oscillation at a frequency proportional to the energy gap. To avoid requiring *a priori* knowledge of the LMG eigenstates (which would be an issue in more complicated models), we modify this protocol to include adiabatic state preparation. We start by preparing equal superpositions of LMG eigenstates in the limits $h/\gamma_x \ll 1$ and $h/\gamma_x \gg 1$, for which the eigenstates are trivially known, and subsequently ramp the LMG Hamiltonian parameters to their desired values, as depicted in Figures 2b and 2c. The initial states and the direction of the ramp are chosen so as to avoid ramping the system through the critical point at $h/\gamma_x = 1$. The result is an equal superposition of LMG eigenstates for arbitrary h/γ_x , provided that the ramp is slow enough to satisfy the adiabatic approximation (see Methods).

We determine the gap energy from the Ramsey oscillations by computing the Fourier transform of the time-domain signal measured in the experiment, as shown in the right panel of Figure 2d. We see a strong peak in the spectrum, which agrees well with the theoretical value for the gap (vertical dashed line). In Figure 2e we show the results for the even-odd and even-even gaps for $j = 1$

through $j = 4$ across the range $0 \leq h/\gamma_x \leq 2$, where the purple line in the top right panel corresponds to the signal plotted in Figure 2d. In each case we see a strong peak corresponding to the gap energy. These peaks are extracted and plotted on top of the theoretical gap curves in the bottom panel of Figure 2e, and in all cases we see very good agreement between theory and experiment without any fit parameters. As the size of the system is increased, the gaps begin to more closely resemble the theoretical gaps in the thermodynamic limit (red curves in the bottom row of Figure 2e). In some cases (for example, the even-even gaps for $j = 2$ and $j = 3$ in Figure 2e), we also see secondary peaks in the Fourier transform. Because we are simulating a low-dimensional realization of the LMG model, the phase transition at $h/\gamma_x = 1$ is replaced by a minimum in the even-even gap as well as a splitting of the approximate degeneracy of the even-odd gap in the region $h/\gamma_x < 1$ (Figure 2a). When ramping h/γ_x from 0 to a nonzero value above this minimum-gap point, we see spurious excitations arising from a breakdown of the adiabatic approximation, whose exact amplitudes depend upon the detailed dynamics of the system as it passes through this point.

Kibble-Zurek-like dynamics

We study the creation of excitations (defects) as the system is driven across the critical point by a non-adiabatic drive. Building on insights related to the formation of topological defects, Zurek put forward predictions for how the number of excitations should scale with the ramp speed [46–49]. The LMG model does not generally follow this scaling for arbitrary ramps, owing to its long-range (all-to-all) interaction [50]. Notwithstanding, Kibble-Zurek-like experiments remain a valuable tool to probe the non-equilibrium response to fast drives. We investigate this excitation process in Figure 3b for $j = 1$ through $j = 4$ as well as $j = 8$ (discussed further below). The protocol, shown in Figure 3a and detailed in the Methods section, begins by adiabatically preparing the LMG ground state for $h/\gamma_x = 2$. The system is then ramped to $h/\gamma_x = 0$ over a variable time T , after which we measure the population remaining in the instantaneous ground state. We plot this measured population as a function of the ramp speed, $2\pi/(\Omega T)$. For slow ramps we see that the system ends in the final ground state with high fidelity, with an overall loss of contrast for larger spins due to decay. For fast ramps, meanwhile, the overlap with the final ground state is low. As illustrated in Figure 3c, as the system is ramped through the point where the gap reaches a minimum, it can be sequentially excited from the ground state to the subspace of even-parity excited states. For very fast ramps, the fidelity saturates to the overlap between the initial and final LMG eigenstates, indicated by the dotted lines on the right side of Figure 3b. This behavior illustrates how rapid quenches can cause diabatic transitions out of the

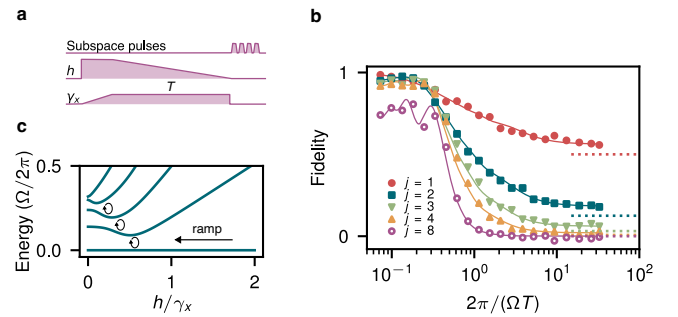


FIG. 3. Transition between adiabatic and impulse regimes. **a**, Experimental protocol for the measurement. We adiabatically prepare the $h/\gamma_x = 2$ ground state, then ramp h to zero over a variable time T . **b**, Experimental results showing the probability that the system ends in the $h/\gamma_x = 0$ eigenstate as a function of ramp speed. The solid curves are single-parameter fits of numerical simulations to the data, where the effect of decoherence is modeled as an exponential decay of the measured population. The dotted lines show the overlaps between the initial and final LMG eigenstates. **c**, Energy spectrum of the even-parity LMG states. When the system is ramped non-adiabatically through the minimum-gap point, it undergoes transitions to the subspace of even-parity excited states.

instantaneous ground state.

The data shown in Figure 3b for $j = 8$ are measured by observing that, if we are only concerned with the dynamics within a subspace of definite parity, there is no need to simulate the opposite-parity subspace. The LMG ground state always has even parity, and because the LMG Hamiltonian is parity-preserving, the state must remain within the even-parity subspace for the duration of the experiment, even if it is excited out of the instantaneous LMG ground state. Therefore, we can double the size of the effective spin in any experiment where we are solely concerned with the even- or odd-parity subspace. We make further use of this idea below.

Statistics of the order parameter

We next turn to the structure of the LMG ground state. The order parameter is $\langle J_x \rangle$. However, for any finite size this will always vanish due to symmetry. To visualize the emergence of the symmetry-broken phase as the spin size increases, we therefore measure the full probability distribution $|\langle 0_{\text{LMG}} | j, m \rangle_x|^2$ of J_x , in the LMG ground state. We can borrow intuition from the classical energy surface of Figure 4a. In the normal phase ($h/\gamma_x > 1$) there is a single minimum at $\theta_0 = 0$, while in the symmetry-broken phase ($h/\gamma_x < 1$) there are two degenerate minima located at $\theta_0 = \pm \arccos(h/\gamma_x)$. Since classically [Eq. (3)] $J_x \sim j \sin \theta$, we expect that $|\langle 0_{\text{LMG}} | j, m \rangle_x|^2$ should be peaked around $m(\theta_0) = j \sin \theta_0$, and the transition from a unimodal to a bimodal distribution can be taken as a finite-size signa-

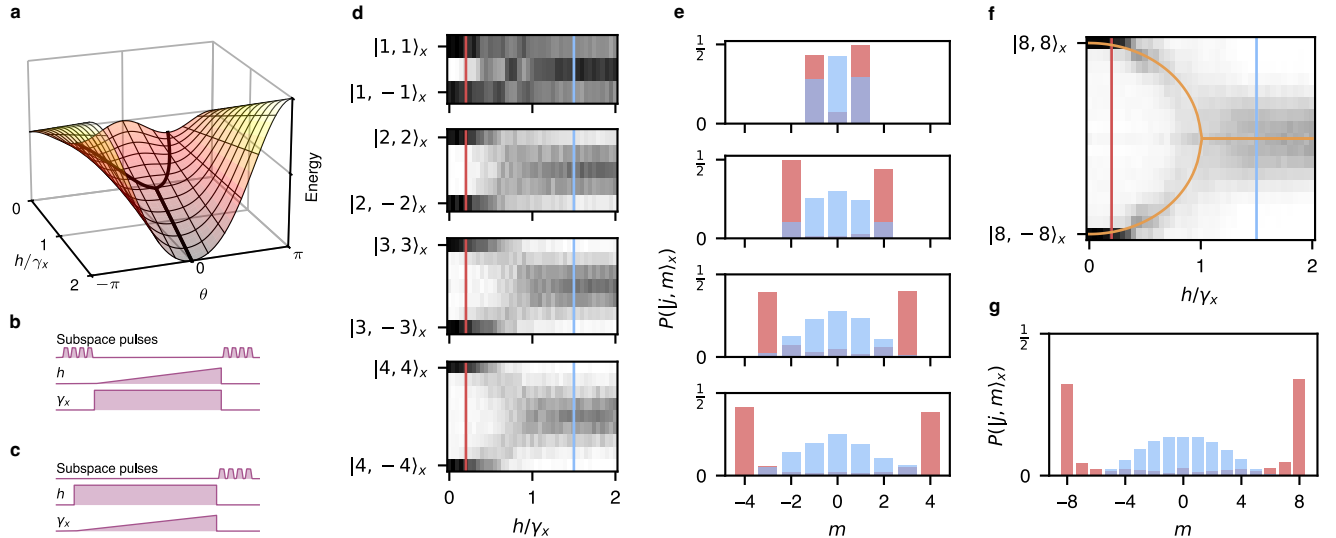


FIG. 4. Distribution of J_x eigenstates in the LMG ground state. **a**, Semiclassical energy surface as a function of θ and h/γ_x , setting $\phi = 0$. In the symmetry-broken phase ($h/\gamma_x < 1$), the energy surface has two degenerate minima. At the critical point ($h/\gamma_x = 1$) these minima merge, and we have a single minimum for $h/\gamma_x > 1$. **b**, Experimental protocol for $h/\gamma_x < 1$. **c**, Experimental protocol for $h/\gamma_x > 1$. In both cases we adiabatically prepare the LMG ground state as described above, then perform a series of pulses mapping one of the J_x eigenstates onto the transmon ground state prior to readout. **d**, Histograms representing the J_x eigenstate distributions as a function of h/γ_x for $j = 1$ through $j = 4$. **e**, J_x eigenstate distributions as a function of h/γ_x for $j = 8$, measured by projecting the J_x eigenstates onto the even-parity subspace and renormalizing. As discussed in the text, the yellow curves give the locations of the minima of the classical energy surface when projected onto the J_x axis. **g**, J_x eigenstate distributions for the particular values of h/γ_x indicated by the vertical lines in **f**.

ture of the broken symmetry. By measuring the distribution of J_x eigenstates we can therefore directly compare the quantum and semiclassical pictures.

The protocol for this measurement in the case where $h/\gamma_x < 1$ is shown in Figure 4b, while that for $h/\gamma_x > 1$ is shown in Figure 4c. In either case, we adiabatically prepare the LMG ground state in a manner analogous to that discussed above, then apply a series of pulses mapping a single J_x eigenstate $|j, m\rangle_x$ onto the transmon ground state. Measuring the population in the transmon ground state yields the overlap $|\langle 0_{\text{LMG}} | j, m \rangle_x|^2$, and we repeat this for all $|j, m\rangle_x$ to measure the full distribution. In Figure 4d we show the distribution across a range of h/γ_x , while in Figure 4e we show it for two specific h/γ_x values, indicated by the vertical lines in Figure 4d. As $h/\gamma_x \rightarrow 0$, recall that the ground state becomes $|j, j\rangle_+ = \frac{1}{\sqrt{2}}(|j, j\rangle_x + |j, -j\rangle_x)$. We therefore see two peaks in the eigenstate distribution at its extreme values. As h/γ_x is increased these peaks begin to merge, converging to a single peak centered around $|j, 0\rangle_x$. This can be understood as the ground state approaching the $-J_z$ ground state, $|j, j\rangle$: in the J_x basis, this state is a spin coherent state on the equator of the rotated phase space sphere.

In Figures 4f and 4g we measure the J_x eigenstate distribution for $j = 8$ (see Methods for details). In Figure 4f we also plot the locations of the minima of the classical energy surface projected onto the J_x axis, $m(\theta_0)$, as dis-

cussed above. The semiclassical intuition is reproduced in this case, in the sense that the centers of the peaks in the distribution qualitatively agree with the semiclassical prediction. If we were to increase j further, the relative widths of the peaks would decrease, ultimately approaching delta functions centered on the locations predicted by the semiclassical analysis.

Excited-state quantum phase transition

In our final experiment we investigate the excited states of the LMG spectrum. In the thermodynamic limit the LMG model has an excited-state quantum phase transition (ESQPT) [51–53] when $h/\gamma_x < 1$, the signature of which is a divergence in its density of states [17, 18, 54, 55]. We present a semiclassical calculation of the density of states, as well as a discussion of its interpretation, in the Supplemental Material. In the small- j regime this divergence is replaced by a splitting of the approximate degeneracy between pairs of even- and odd-parity states. In Figure 5a we show the spectrum of the LMG Hamiltonian for $j = 8$. The red curve indicates the energy difference between the peak of the barrier and the minimum of the semiclassical energy surface as a function of h/γ_x , which we henceforth call the critical energy $E_c(h)$. When the eigenenergy is below $E_c(h)$, pairs of even- and odd-parity states are nearly degenerate. The

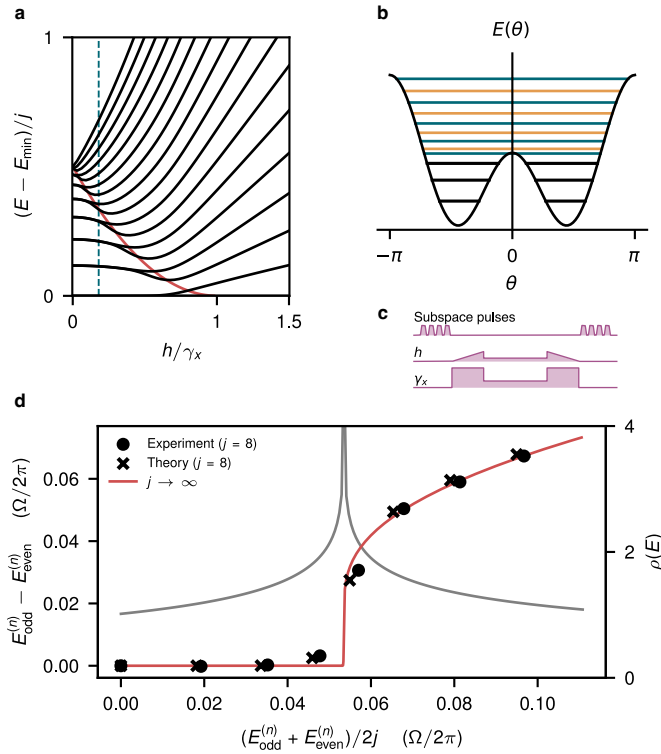


FIG. 5. Excited-state quantum phase transition (ESQPT). **a**, LMG energy spectrum as a function of h/γ_x for $j = 8$. The red curve indicates the critical energy $E_c(h)$ of the ESQPT, equal to the height of the barrier of the classical energy surface relative to its minimum energy. **b**, Semiclassical energy surface for $h/\gamma_x = 0.18$ (vertical dashed line in **a**), with $\phi = 0$. The horizontal lines show the $j = 8$ eigenenergies. For energies near or above $E_c(h)$, we plot even-parity eigenenergies in blue and odd-parity eigenenergies in yellow. **c**, Experimental protocol. We measure energy gaps between adjacent states of like parity in a manner analogous to the gap measurement in Figure 2. Here, however, we use a different energy scale Ω during the ramps in order to more easily satisfy the adiabatic approximation (see Methods). **d**, Experimental results for the energy difference of each even-odd pair as a function of that pair's average energy, along with the theoretical expectation for $j = 8$, as measured here, and $j \rightarrow \infty$. We also show the semiclassical density of states result in gray.

energies of these states separate when they are roughly equal to $E_c(h)$. This is shown in Figure 5b, where we plot the $j = 8$ spectrum at $h/\gamma_x = 0.18$ on top of the semiclassical energy surface.

We experimentally investigate this behavior by measuring the full energy spectrum of the LMG Hamiltonian for $h/\gamma_x = 0.18$ and $j = 8$. We begin by noting that, to a very good approximation, the lowest even-odd energy gap is $E_{|1_{\text{LMG}}} - E_{|0_{\text{LMG}}} \approx 0$ for the h/γ_x considered here. This can be inferred from the even-odd gap results in Figure 2. We perform a series of gap measurements similar to those in Figure 2, first measuring every even-even gap $E_{|2(n+1)_{\text{LMG}}} - E_{|(2n)_{\text{LMG}}}$, then measuring every odd-odd gap $E_{|(2(n+1)+1)_{\text{LMG}}} - E_{|(2n+1)_{\text{LMG}}}$.

From these energy differences, along with the fact that $E_{|1_{\text{LMG}}} - E_{|0_{\text{LMG}}} \approx 0$, we reconstruct the full energy spectrum for $j = 8$ despite the fact that we cannot directly simulate a spin this large. The protocol, shown in Figure 5c and discussed in the Methods section, is analogous to that for the gap measurements in Figure 2.

The results of this experiment are shown in Figure 5d. We plot the reconstructed energy splitting for each even-odd pair as a function of the average energy of that pair. We show the prediction for the splitting as $j \rightarrow \infty$, as well as the semiclassical density of states. Below the critical energy $E_c(h)$, the even-odd pairs are degenerate for $j \rightarrow \infty$, and nearly degenerate for $j = 8$. When the energy is above $E_c(h)$ the degeneracy is lifted, and the experimental data for $j = 8$ agree well with the theoretical values for $j = 8$ and $j \rightarrow \infty$, where the sharp change in the latter is indicative of an excited-state quantum phase transition.

DISCUSSION

In this paper we presented the results of analog quantum simulations of the LMG model in a superconducting transmon qudit using up to $d = 9$ levels, realizing an effective spin of size $j = 4$ or, in cases involving states of definite parity, $j = 8$. Our implementation of the LMG Hamiltonian is fully tunable, permitting the study of the system's behavior for any (potentially time-dependent) ratio of h/γ_x , without breaking parity symmetry. Furthermore, our methods enable the study of ground and excited states, energy gaps, dynamics, order parameters, and other signatures of quantum criticality without prior knowledge of the system's eigenstates.

This experimental progress comes at an opportune time. In recent years there have been a number of proposals for useful qudit-based quantum simulations, particularly in lattice gauge theory [6–12]. Qudit-based models are also of interest in the areas of quantum chemistry [13] and quantum criticality [14]. As demonstrated by our results, the flexible and high-fidelity control afforded to transmon qudits makes them an ideal platform for the experimental realization of these proposals. The high E_J/E_C ratio of the transmon used in this work is achieved through minor modifications of the device geometry [28], and it is therefore compatible with state-of-the-art large-scale superconducting processor architectures. We note that, unlike qudit platforms that make use of natural multi-level quantum systems (e.g., trapped ions [19, 20] or nuclear spins [21, 22]), a transmon qudit processor can be engineered to optimize the tradeoff between dimensionality and anharmonicity required for a particular simulation [28]. The connectivity of the processor can also be designed with the simulated Hamiltonian in mind, and recent advances in tailoring interactions between transmon qudits [24–26] suggest that this platform can be scaled to multi-qudit systems. Our results thus open the door for efficient quantum simulations of com-

plex and practically relevant qudit-based models.

I. ACKNOWLEDGMENTS

This material is based upon work supported by the Air Force Office of Scientific Research under Award No. FA9550-23-1-0121. Devices were fabricated and provided by the Superconducting Qubits at Lincoln Laboratory (SQUILL) Foundry at MIT Lincoln Laboratory, with funding from the Laboratory for Physical Sciences (LPS) Qubit Collaboratory. The traveling-wave parametric amplifier (TWPA) used in this experiment was provided by IARPA and Lincoln Labs.

II. METHODS

Drive Hamiltonian. We write the bare transmon Hamiltonian in the lab frame as

$$H_0 = \sum_{n=0}^{d-1} \omega_n |n\rangle \langle n|. \quad (6)$$

The lowest transition frequency in our system is $(\omega_1 - \omega_0)/2\pi = 4.870$ GHz, and the anharmonicity is $|\alpha|/2\pi = 104$ MHz; see the Supplemental Materials for the full list of device parameters. We drive the transmon with

$$H_{\text{drive}}(t) = \sum_{k=1}^{d-1} V^{(k)}(t) \sum_{n=1}^{d-1} \gamma_n \left(|n-1\rangle \langle n| + |n\rangle \langle n-1| \right), \quad (7)$$

consisting of $d-1$ simultaneous drives $V^{(k)}(t) = \mathcal{E}^{(k)}(t) \cos(\omega^{(k)}(t)t + \phi^{(k)}(t))$, with γ_n being the transmon charge matrix elements. The drive strengths, frequencies, and phases of all drives are potentially time-dependent. We set each drive frequency $\omega^{(k)}$ to be detuned from the $|k-1\rangle \leftrightarrow |k\rangle$ transition by a small amount: $\omega^{(k)}(t) = (\omega_k - \omega_{k-1}) - (\Delta_k(t) - \Delta_{k-1}(t))$. Transforming to a rotating frame defined by time-dependent detunings,

$$R(t) = \exp \left[i \sum_{n=0}^{d-1} \left(\omega_n - \int_0^t dt' \Delta_n(t') \right) |n\rangle \langle n| \right], \quad (8)$$

changes the total lab-frame Hamiltonian $H_{\text{lab}}(t) = H_0 + H_{\text{drive}}(t)$ to

$$H_{\text{rot}}(t) = R(t) H_{\text{lab}}(t) R^\dagger(t) + i \left(\frac{d}{dt} R(t) \right) R^\dagger(t). \quad (9)$$

It is helpful here to define the total accumulated phase relative to the bare transmon frame,

$$A_n(t) \equiv \int_0^t dt' \Delta_n(t'), \quad (10)$$

as well as the complex-valued drive strength

$$\Omega_n(t) \equiv \frac{1}{2} \gamma_n \mathcal{E}^{(n)}(t) e^{i\phi^{(n)}(t)}. \quad (11)$$

We apply the frame transformation and take the rotating wave approximation (RWA) by neglecting terms rotating at the anharmonicity $|\alpha|$ or faster to obtain

$$H_{\text{rot}}(t) = \sum_{n=0}^{d-1} \Delta_n(t) |n\rangle \langle n| + \sum_{n=1}^{d-1} \left(\Omega_n(t) e^{i\zeta_n(t)} |n-1\rangle \langle n| + \text{H.c.} \right) \quad (12)$$

where

$$\zeta_n(t) = (\Delta_n(t) - \Delta_{n-1}(t))t - (A_n(t) - A_{n-1}(t)). \quad (13)$$

In the case where the detunings are constant, $\zeta_n(t) = 0$. On the other hand, in the case where the detunings change with respect to time, as they do during the adiabatic ramps, $\zeta_n(t)$ introduces a problematic phase shift on the drives. We compensate for this by setting the time-dependent phase of each drive to $\phi^{(n)}(t) = -\zeta_n(t)$. In this way we arrive at the effective Hamiltonian in Eq. 5, yielding an explicit solution for the drive strengths, frequencies, and phases needed to realize H_{LMG} for any time-dependent h and γ_x .

Drive generation. In practice we produce the simultaneous drive tones by modulating a single local oscillator (LO) tone with $d-1$ fixed-frequency modulation tones via single-sideband mixing. In what follows we refer to the resulting upconverted frequencies as “reference frequencies” because they serve as the phase references for each transition. When the detunings are constant, $\Delta_n(t) = \Delta_n$, we choose reference frequencies $\beta_n = (\omega_n - \omega_{n-1}) - (\Delta_n - \Delta_{n-1})$. The frame tracked by these reference frequencies is therefore the one yielding the diagonal elements of Eq. 5, and the off-diagonal elements are simply given by the strengths of the drives.

The situation is more complicated when the detunings are time-dependent. In this case, because we cannot smoothly vary the reference frequencies in the hardware, we instead fix them to the values given by the initial detunings: $\beta_n = (\omega_n - \omega_{n-1}) - (\Delta_n(0) - \Delta_{n-1}(0))$. Recall that the desired waveform is given in the lab frame by

$$V^{(n)}(t) = \mathcal{E}^{(n)}(t) \cos(\omega^{(n)}(t)t + \phi^{(n)}(t)). \quad (14)$$

We emphasize that the time-dependent strengths, frequencies, and phases of these drives are determined by a direct comparison of Eq. 5 to the desired LMG Hamiltonian. We split each drive tone into a rapidly oscillating component at $\omega^{(n)}(0) = \beta_n$ and a slowly oscillating component:

$$\begin{aligned} V^{(n)}(t) &= \mathcal{E}^{(n)}(t) [\cos(\beta_n t) \cos(\delta\omega^{(n)}(t)t + \phi^{(n)}(t)) \\ &\quad - \sin(\beta_n t) \sin(\delta\omega^{(n)}(t)t + \phi^{(n)}(t))] \\ &\equiv \cos(\beta_n t) v_I^{(n)}(t) - \sin(\beta_n t) v_Q^{(n)}(t), \end{aligned} \quad (15)$$

where $\delta\omega^{(n)}(t) = \omega^{(n)}(t) - \omega^{(n)}(0) = \omega^{(n)}(t) - \beta_n$. Therefore, by applying time-dependent envelopes $v_I^{(n)}(t)$ and $v_Q^{(n)}(t)$ to the in-phase and quadrature components of the modulation tones, we realize the desired upconverted signal despite the fact that each reference frequency is, in reality, fixed to a single value for the duration of the pulse. The final step is to correct the reference frame itself such that the frame tracked by the reference oscillators β_n coincides with the desired frame rotation $R(t)$. This correction amounts to a single instantaneous update of each modulation frequency to its new value at the end of the pulse, as well as a single instantaneous update of the phase of each modulation tone to account for the accumulated phase shift $\phi^{(n)}(t) - \phi^{(n)}(0)$.

Protocols. In this section we discuss the details of the various experimental protocols used throughout this work.

1. *Dynamical phase transition* (Figure 1f): For the case where the system begins in $|4, 4\rangle$ (transmon state $|0\rangle$), we simply turn on the LMG drives as described in the main text for a variable time t . Following this we measure the qudit state (Supplemental Material) and plot the resulting populations. For the case where the system begins in $|4, 3\rangle$ (transmon state $|5\rangle$), we apply sequential π pulses between pairs of adjacent levels to prepare the initial state prior to turning on the LMG drives.
2. *Gap measurement* (Figure 2): Due to the presence of the second-order phase transition at $h/\gamma_x = 1$, we consider the cases where $h/\gamma_x < 1$ and $h/\gamma_x > 1$ separately. We note that this protocol can be extended to the case where the critical point is not known (see below). The protocol for $h/\gamma_x < 1$ is depicted in Figure 2b. Beginning in the ground state, we apply sequential pulses between adjacent transmon levels to prepare equal superpositions of the $|j, m\rangle_{\pm}$ states, defined above as the definite-parity eigenstates of J_x^2 . In particular, for the even-odd gap we prepare $\frac{1}{\sqrt{2}}(|j, j\rangle_+ + |j, j\rangle_-)$, while for the even-even gap we prepare $\frac{1}{\sqrt{2}}(|j, j\rangle_+ + |j, j-1\rangle_+)$. Next we turn on the LMG Hamiltonian drives with initial parameters of $\gamma_x = 1$ and $h = 0$, and slowly ramp h to its target value. In the limit where this process is adiabatic, the resulting state will be an equal superposition of the instantaneous LMG eigenstates at the end of the ramp. We allow the system to evolve for a variable time Δt before ramping h back to 0, turning off the LMG drives, and inverting the initial state preparation pulse sequence. Finally, we measure the population in the transmon ground state and plot it as a function of time, as shown in Figure 2d. We note that although the superposition state will accumulate a relative phase during the ramps at a rate given by the instantaneous energy difference between the states, the ramp duration is kept fixed for all time points within a single gap measurement (in this case the ramp duration is $2\mu\text{s}$). The result is an overall phase shift in the oscillation, which does not affect the gap energy estimate.
3. *Kibble-Zurek* (Figure 3): This protocol begins with the system in the state $|j, j\rangle$, i.e., the ground state of $-J_z$. We turn on the LMG drives with $h = 2$ and γ_x initially set to 0, then ramp γ_x to 1 over the course of 200 ns. Because the gap is large for the duration of this ramp, we faithfully prepare the LMG ground state for $h/\gamma_x = 2$. Following this, we ramp h down from 2 to 0 over a variable time T . In the limit of large T this process will be adiabatic, and so we should have prepared the LMG ground state for $h/\gamma_x = 0$, which due to parity conservation we know to be the $|j, j\rangle_+$ given above. We apply sequential pulses to each transition to map this state onto the transmon ground state, measure the transmon ground state population, and plot it as a function of ramp speed $2\pi/(\Omega T)$ in Figure 3b.
4. *Statistics of the order parameter* (Figure 4):

In Figures 4f and 4g we make use of the fact that the LMG ground state has even parity to measure the distribution of J_x eigenstates. To do this we note that, defining a projector P_e onto the even subspace, the LMG ground state is unaffected by this projector: $P_e |0_{\text{LMG}}\rangle = |0_{\text{LMG}}\rangle$. The overlap of the LMG ground state with a J_x eigenstate $|j, m\rangle_x$, then, is

$$|\langle 0_{\text{LMG}} | j, m \rangle_x|^2 = |\langle 0_{\text{LMG}} | P_e | j, m \rangle_x|^2 = \mathcal{N} |\langle 0_{\text{LMG}} | \psi_m \rangle|^2 \quad (16)$$

where $|\psi_m\rangle = \frac{1}{\sqrt{\mathcal{N}}} P_e |j, m\rangle_x$ and $\mathcal{N} = \langle j, m | P_e | j, m \rangle_x$ is a normalization factor. We therefore measure the overlap of $|0_{\text{LMG}}\rangle$ with each of the $|\psi_m\rangle$ and renormalize the resulting populations to yield the J_x eigenstate distribution of this larger effective spin.

5. *Excited-state quantum phase transition* (Figure 5): This protocol is similar to that for the gap experiments in Figure 2. The key differences are: (1) we

neglect the subspace with the opposite parity from the one we are measuring; (2) we must prepare different initial superpositions prior to the adiabatic ramps; and (3) the adiabatic approximation is more difficult to satisfy because the energy gaps will, in general, become smaller with increasing energy. We address this final point by observing that we are free to use different energy scales Ω for different parts of the protocol. In particular, during the adiabatic ramps we increase it to $\Omega/(2\pi) = 5.730$ MHz while keeping the ramp duration fixed to 2 μs . This choice has the effect of increasing the energy gaps, permitting a more adiabatic ramp while mitigating the decoherence that would result from simply increasing the ramp duration. We note that this strategy comes at the potential cost of more coherent error due to a breakdown of the RWA, and the value of Ω used here is chosen to balance the various sources of error. During the constant-Hamiltonian part of the protocol, meanwhile, the adiabatic condition is not relevant, and we therefore return the energy scale to $\Omega/(2\pi) = 1.910$ MHz.

[1] Georgescu, I., Ashhab, S. & Nori, F. Quantum simulation. *Reviews of Modern Physics* **86**, 153–185 (2014). URL <https://link.aps.org/doi/10.1103/RevModPhys.86.153>. Publisher: American Physical Society.

[2] Daley, A. J. *et al.* Practical quantum advantage in quantum simulation. *Nature* **607**, 667–676 (2022). URL <https://www.nature.com/articles/s41586-022-04940-6>. Publisher: Nature Publishing Group.

[3] Evered, S. J. *et al.* Probing the Kitaev honeycomb model on a neutral-atom quantum computer. *Nature* **645**, 341–347 (2025). URL <https://www.nature.com/articles/s41586-025-09475-0>. Publisher: Nature Publishing Group.

[4] González-Cuadra, D. *et al.* Observation of string breaking on a (2 + 1)D Rydberg quantum simulator. *Nature* **642**, 321–326 (2025). URL <https://www.nature.com/articles/s41586-025-09051-6>. Publisher: Nature Publishing Group.

[5] Andersen, T. I. *et al.* Thermalization and criticality on an analogue-digital quantum simulator. *Nature* **638**, 79–85 (2025). URL <https://www.nature.com/articles/s41586-024-08460-3>. Publisher: Nature Publishing Group.

[6] Ciavarella, A., Klco, N. & Savage, M. J. Trailhead for quantum simulation of SU(3) Yang-Mills lattice gauge theory in the local multiplet basis. *Physical Review D* **103**, 094501 (2021). URL <https://link.aps.org/doi/10.1103/PhysRevD.103.094501>. Publisher: American Physical Society.

[7] Gustafson, E. J. Prospects for simulating a qudit-based model of \$(1+1)\backslashmathrm{D}\$ scalar QED. *Physical Review D* **103**, 114505 (2021). URL <https://link.aps.org/doi/10.1103/PhysRevD.103.114505>. Publisher: American Physical Society.

[8] González-Cuadra, D., Zache, T. V., Carrasco, J., Kraus, B. & Zoller, P. Hardware Efficient Quantum Simulation of Non-Abelian Gauge Theories with Qudits on Rydberg Platforms. *Physical Review Letters* **129**, 160501 (2022). URL <https://link.aps.org/doi/10.1103/PhysRevLett.129.160501>. Publisher: American Physical Society.

[9] Zache, T. V., González-Cuadra, D. & Zoller, P. Fermion-qudit quantum processors for simulating lattice gauge theories with matter. *Quantum* **7**, 1140 (2023). URL <https://quantum-journal.org/papers/q-2023-10-16-1140/>. Publisher: Verein zur Förderung des Open Access Publizierens in den Quantenwissenschaften.

[10] Illa, M., Robin, C. E. & Savage, M. J. Qu8its for quantum simulations of lattice quantum chromodynamics. *Physical Review D* **110**, 014507 (2024). URL <https://link.aps.org/doi/10.1103/PhysRevD.110.014507>. Publisher: American Physical Society.

[11] Meth, M. *et al.* Simulating two-dimensional lattice gauge theories on a qudit quantum computer. *Nature Physics* **21**, 570–576 (2025). URL <https://www.nature.com/articles/s41567-025-02797-w>. Publisher: Nature Publishing Group.

[12] Calliari, G., Di Liberto, M., Pichler, H. & Zache, T. V. Quantum Simulating Continuum Field Theories with Large-Spin Lattice Models. *PRX Quantum* **6**, 030304 (2025). URL <https://link.aps.org/doi/10.1103/nt76-ttmj>. Publisher: American Physical Society.

[13] MacDonell, R. J. *et al.* Analog quantum simulation of chemical dynamics. *Chemical Science* **12**, 9794–9805 (2021). URL <https://pubs.rsc.org/en/content/>

articlelanding/2021/sc/d1sc02142g. Publisher: The Royal Society of Chemistry.

[14] Pausch, L., Damanet, F., Bastin, T. & Martin, J. Dissipative phase transition: From qubits to qudits. *Physical Review A* **110**, 062208 (2024). URL <https://link.aps.org/doi/10.1103/PhysRevA.110.062208>. Publisher: American Physical Society.

[15] Lipkin, H. J., Meshkov, N. & Glick, A. J. Validity of many-body approximation methods for a solvable model. (I). Exact solutions and perturbation theory. *Nuclear Physics* **62**, 188–198 (1965). URL <https://ui.adsabs.harvard.edu/abs/1965NucPh..62..188L>.

[16] Castaños, O., López-Peña, R., Hirsch, J. G. & López-Moreno, E. Classical and quantum phase transitions in the Lipkin-Meshkov-Glick model. *Physical Review B* **74**, 104118 (2006). URL <https://link.aps.org/doi/10.1103/PhysRevB.74.104118>. Publisher: American Physical Society.

[17] Ribeiro, P., Vidal, J. & Mosseri, R. Thermodynamical Limit of the Lipkin-Meshkov-Glick Model. *Physical Review Letters* **99** (2007). URL <https://link.aps.org/doi/10.1103/PhysRevLett.99.050402>. Publisher: American Physical Society (APS).

[18] Ribeiro, P., Vidal, J. & Mosseri, R. Exact spectrum of the Lipkin-Meshkov-Glick model in the thermodynamic limit and finite-size corrections. *Physical Review E* **78** (2008). URL <https://link.aps.org/doi/10.1103/PhysRevE.78.021106>. Publisher: American Physical Society (APS).

[19] Ringbauer, M. *et al.* A universal qudit quantum processor with trapped ions. *Nature Physics* **18**, 1053–1057 (2022). URL <https://www.nature.com/articles/s41567-022-01658-0>. Publisher: Nature Publishing Group.

[20] Low, P. J., White, B. & Senko, C. Control and readout of a 13-level trapped ion qudit. *npj Quantum Information* **11**, 85 (2025). URL <https://www.nature.com/articles/s41534-025-01031-y>. Publisher: Nature Publishing Group.

[21] Yu, X. *et al.* Schrödinger cat states of a nuclear spin qudit in silicon. *Nature Physics* **21**, 362–367 (2025). URL <https://www.nature.com/articles/s41567-024-02745-0>. Publisher: Nature Publishing Group.

[22] Vaartjes, A. *et al.* Certifying the quantumness of a nuclear spin qudit through its uniform precession. *Newton* **1** (2025). URL [https://www.cell.com/newton/abstract/S2950-6360\(25\)00009-X](https://www.cell.com/newton/abstract/S2950-6360(25)00009-X). Publisher: Elsevier.

[23] Blok, M. *et al.* Quantum Information Scrambling on a Superconducting Qutrit Processor. *Physical Review X* **11**, 021010 (2021). URL <https://link.aps.org/doi/10.1103/PhysRevX.11.021010>.

[24] Morvan, A. *et al.* Qutrit Randomized Benchmarking. *Physical Review Letters* **126**, 210504 (2021). URL <https://link.aps.org/doi/10.1103/PhysRevLett.126.210504>.

[25] Goss, N. *et al.* High-fidelity qutrit entangling gates for superconducting circuits. *Nature Communications* **13**, 7481 (2022). URL <https://www.nature.com/articles/s41467-022-34851-z>.

[26] Nguyen, L. B. *et al.* Empowering a qudit-based quantum processor by traversing the dual bosonic ladder. *Nature Communications* **15**, 7117 (2024). URL <https://www.nature.com/articles/s41467-024-51434-2>. Publisher: Nature Publishing Group.

[27] Liu, P. *et al.* Performing SU (d) Operations and Rudimentary Algorithms in a Superconducting Transmon Qudit for d = 3 and d = 4. *Physical Review X* **13**, 021028 (2023). URL <https://link.aps.org/doi/10.1103/PhysRevX.13.021028>.

[28] Wang, Z., Parker, R. W., Champion, E. & Blok, M. S. High-\$\{E\}\cdot\{J\}\cdot\{E\}\cdot\{C\}\$ transmon qudits with up to 12 levels. *Physical Review Applied* **23**, 034046 (2025). URL <https://link.aps.org/doi/10.1103/PhysRevApplied.23.034046>. Publisher: American Physical Society.

[29] Senko, C. *et al.* Realization of a Quantum Integer-Spin Chain with Controllable Interactions. *Physical Review X* **5**, 021026 (2015). URL <https://link.aps.org/doi/10.1103/PhysRevX.5.021026>. Publisher: American Physical Society.

[30] Edmunds, C. *et al.* Symmetry-Protected Topological Haldane Phase on a Qudit Quantum Processor. *PRX Quantum* **6**, 020349 (2025). URL <https://link.aps.org/doi/10.1103/PRXQuantum.6.020349>. Publisher: American Physical Society.

[31] Wang, Y., Snizhko, K., Romito, A., Gefen, Y. & Murch, K. Dissipative preparation and stabilization of many-body quantum states in a superconducting qutrit array. *Physical Review A* **108**, 013712 (2023). URL <https://link.aps.org/doi/10.1103/PhysRevA.108.013712>. Publisher: American Physical Society.

[32] Kumaran, K. *et al.* Transmon qutrit-based simulation of spin-1 AKLT systems (2025). URL <https://arxiv.org/abs/2412.19786>. ArXiv:2412.19786 [quant-ph].

[33] Wang, Z. T. *et al.* Observing Two-Particle Correlation Dynamics in Tunable Superconducting Bose-Hubbard Simulators (2025). URL <https://arxiv.org/abs/2509.02180>. ArXiv:2509.02180 [quant-ph].

[34] Champion, E., Wang, Z., Parker, R. W. & Blok, M. S. Efficient Control of a Transmon Qudit Using Effective Spin-\$\frac{7}{2}\$ Rotations. *Physical Review X* **15**, 021096 (2025). URL <https://link.aps.org/doi/10.1103/vbh4-lysv>. Publisher: American Physical Society.

[35] Kitagawa, M. & Ueda, M. Squeezed spin states. *Physical Review A* **47**, 5138–5143 (1993). URL <https://link.aps.org/doi/10.1103/PhysRevA.47.5138>. Publisher: American Physical Society.

[36] Koch, J. *et al.* Charge-insensitive qubit design derived from the Cooper pair box. *Physical Review A* **76**, 042319 (2007). URL <https://link.aps.org/doi/10.1103/PhysRevA.76.042319>.

[37] Blais, A., Grimsmo, A. L., Girvin, S. & Wallraff, A. Circuit quantum electrodynamics. *Reviews of Modern Physics* **93**, 025005 (2021). URL <https://link.aps.org/doi/10.1103/RevModPhys.93.025005>.

[38] Heyl, M., Polkovnikov, A. & Kehrein, S. Dynamical Quantum Phase Transitions in the Transverse-Field Ising Model. *Physical Review Letters* **110**, 135704 (2013). URL <https://link.aps.org/doi/10.1103/PhysRevLett.110.135704>. Publisher: American Physical Society.

[39] Heyl, M. Dynamical Quantum Phase Transitions in Systems with Broken-Symmetry Phases. *Physical Review Letters* **113**, 205701 (2014). URL <https://link.aps.org/doi/10.1103/PhysRevLett.113.205701>. Publisher: American Physical Society.

[40] Jafari, R. & Johannesson, H. Loschmidt Echo Revivals: Critical and Noncritical. *Physical Review Letters* **118**, 015701 (2017). URL <https://link.aps.org/doi/10.1103/PhysRevLett.118.015701>. Publisher: American Physical Society.

[41] Cejnar, P. & Stránský, P. Impact of quantum phase transitions on excited-level dynamics. *Physical Review E* **78**, 031130 (2008). URL <https://link.aps.org/doi/10.1103/PhysRevE.78.031130>. Publisher: American Physical Society.

[42] Puebla, R. Finite-component dynamical quantum phase transitions. *Physical Review B* **102**, 220302 (2020). URL <https://link.aps.org/doi/10.1103/PhysRevB.102.220302>. Publisher: American Physical Society.

[43] Santos, L. F. & Pérez-Bernal, F. Structure of eigenstates and quench dynamics at an excited-state quantum phase transition. *Physical Review A* **92**, 050101 (2015). URL <https://link.aps.org/doi/10.1103/PhysRevA.92.050101>. Publisher: American Physical Society.

[44] Campbell, S. Criticality revealed through quench dynamics in the Lipkin-Meshkov-Glick model. *Physical Review B* **94**, 184403 (2016). URL <https://link.aps.org/doi/10.1103/PhysRevB.94.184403>. Publisher: American Physical Society.

[45] Fogarty, T., Deffner, S., Busch, T. & Campbell, S. Orthogonality Catastrophe as a Consequence of the Quantum Speed Limit. *Physical Review Letters* **124**, 110601 (2020). URL <https://link.aps.org/doi/10.1103/PhysRevLett.124.110601>. Publisher: American Physical Society.

[46] Zurek, W. H. Cosmological experiments in superfluid helium? *Nature* **317**, 505–508 (1985). URL <https://www.nature.com/articles/317505a0>. Publisher: Nature Publishing Group.

[47] Zurek, W. H., Dorner, U. & Zoller, P. Dynamics of a Quantum Phase Transition. *Physical Review Letters* **95**, 105701 (2005). URL <https://link.aps.org/doi/10.1103/PhysRevLett.95.105701>. Publisher: American Physical Society.

[48] Dziarmaga, J. Dynamics of a Quantum Phase Transition: Exact Solution of the Quantum Ising Model. *Physical Review Letters* **95**, 245701 (2005). URL <https://link.aps.org/doi/10.1103/PhysRevLett.95.245701>. Publisher: American Physical Society.

[49] Damski, B. The Simplest Quantum Model Supporting the Kibble-Zurek Mechanism of Topological Defect Production: Landau-Zener Transitions from a New Perspective. *Physical Review Letters* **95**, 035701 (2005). URL <https://link.aps.org/doi/10.1103/PhysRevLett.95.035701>. Publisher: American Physical Society.

[50] Defenu, N., Enss, T., Kastner, M. & Morigi, G. Dynamical Critical Scaling of Long-Range Interacting Quantum Magnets. *Physical Review Letters* **121**, 240403 (2018). URL <https://link.aps.org/doi/10.1103/PhysRevLett.121.240403>. Publisher: American Physical Society.

[51] Stránský, P., Macek, M. & Cejnar, P. Excited-state quantum phase transitions in systems with two degrees of freedom: Level density, level dynamics, thermal properties. *Annals of Physics* **345**, 73–97 (2014). URL <https://www.sciencedirect.com/science/article/pii/S000349161400061X>.

[52] Puebla, R. & Relaño, A. Non-thermal excited-state quantum phase transitions. *Europhysics Letters* **104**, 50007 (2014). URL <https://doi.org/10.1209/0295-5075/104/50007>. Publisher: EDP Sciences, IOP Publishing and Società Italiana di Fisica.

[53] Cejnar, P., Stránský, P., Macek, M. & Kloc, M. Excited-state quantum phase transitions. *Journal of Physics A: Mathematical and Theoretical* **54**, 133001 (2021). URL <https://doi.org/10.1088/1751-8121/abdf8>. Publisher: IOP Publishing.

[54] Heiss, W. D., Scholtz, F. G. & Geyer, H. B. The large N behaviour of the Lipkin model and exceptional points. *Journal of Physics A: Mathematical and General* **38**, 1843 (2005). URL <https://dx.doi.org/10.1088/0305-4470/38/9/002>.

[55] Leyvraz, F. & Heiss, W. D. Large-NScaling Behavior of the Lipkin-Meshkov-Glick Model. *Physical Review Letters* **95** (2005). URL <https://link.aps.org/doi/10.1103/PhysRevLett.95.050402>. Publisher: American Physical Society (APS).

Supplemental Material: Analog quantum simulation of the Lipkin-Meshkov-Glick model in a transmon qudit

Elizabeth Champion,^{1,2} Annie Schwartz,^{1,2} Muhammad A. Ijaz,^{1,2} Xiaohui Xu,^{1,2} Steve Campbell,^{3,4} Gabriel T. Landi,^{1,2} and Machiel Blok^{1,2,*}

¹*Department of Physics and Astronomy, University of Rochester, Rochester, New York 14627, USA*

²*University of Rochester Center for Coherence and Quantum Science, Rochester, New York 14627, USA*

³*School of Physics, University College Dublin, Belfield, Dublin 4, Ireland*

⁴*Centre for Quantum Engineering, Science, and Technology, University College Dublin, Dublin 4, Ireland*

(Dated: December 8, 2025)

CONTENTS

I. High- E_J/E_C transmon device	1
II. LMG eigenstates	2
III. Semiclassical model	3
A. Classical energy surface and ground state solutions	3
B. Density of states	4
References	7

I. HIGH- E_J/E_C TRANSMON DEVICE

The experiments presented in this work employed a superconducting qudit device with sufficiently many accessible levels to emulate the large spin. For this purpose we use a transmon qudit with a large ratio of $E_J/E_C \approx 300$, where E_J is the Josephson energy and E_C is the capacitive energy [1, 2]. We provide the device parameters in Table S1. We perform single-shot readout of the qudit using a multi-tone readout protocol in which a dispersively coupled resonator is probed at three frequencies simultaneously [3, 4]. In Figure S1 we report measured values for T_1 , T_2^{Ramsey} , and T_2^{Echo} for every transition used in this work. Each coherence time is measured 120 times over the course of roughly 20 hours, and we show histograms of the measured times; the numerical values reported in the Figure are the means and standard deviations across this data set.

We refer the reader to Ref. [3], in which the transmon used here is labeled Q_5 , for an in-depth discussion of the device, its noise properties, and the multi-tone readout protocol. We note that the experiments in this work were performed during a different cooldown from those in Ref. [3], which accounts for the slight discrepancies between the device parameters and coherence times reported here and those reported in earlier work.

f_{01}	f_{12}	f_{23}	f_{34}	f_{45}	f_{56}	f_{67}	f_{78}	E_J	E_C	f_r	g
4.870	4.766	4.658	4.544	4.424	4.298	4.163	4.020	30.497	0.102	6.471	0.029

TABLE S1. Measured transition frequencies and calculated E_J , E_C , bare resonator frequency f_r , and coupling strength g . All values are expressed in GHz.

* machielblok@rochester.edu

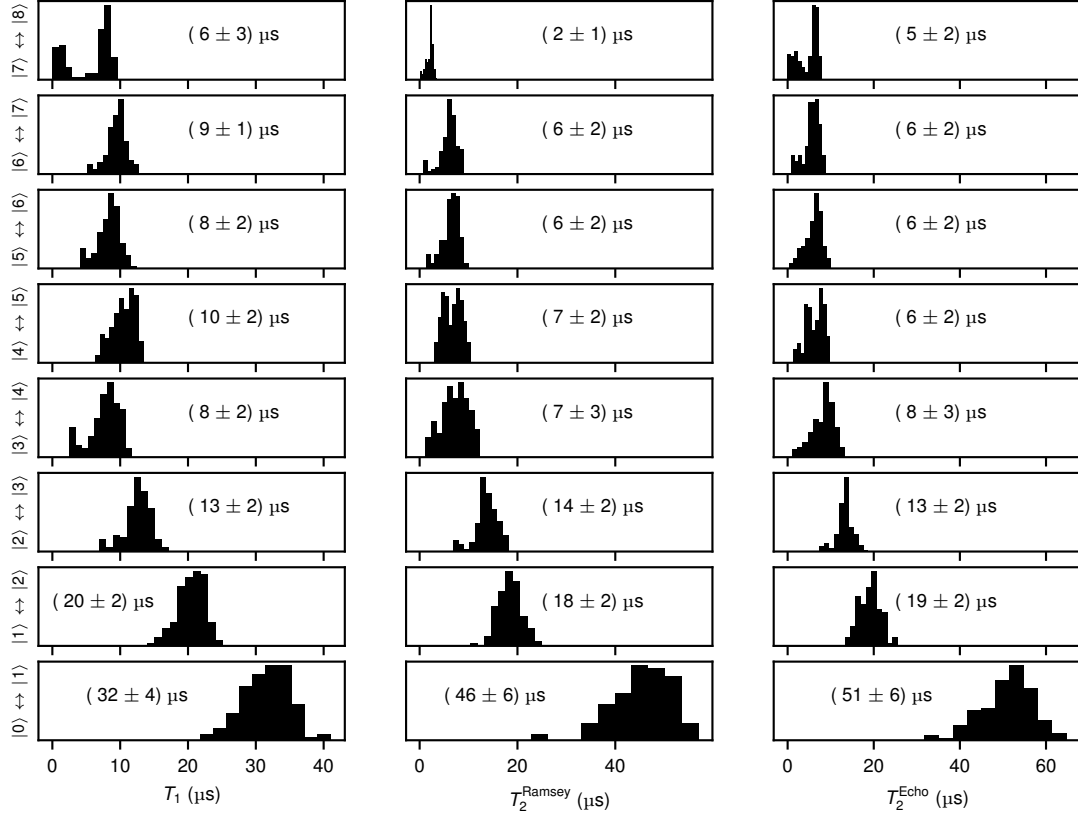


FIG. S1. Histograms of measured coherence times for 120 repetitions over the course of roughly 20 hours. The numerical values reported in each panel are means and standard deviations.

II. LMG EIGENSTATES

The LMG Hamiltonian we simulate in this work is given by

$$H_{\text{LMG}}/\Omega = -hJ_z - \frac{\gamma_x}{2j}J_x^2. \quad (\text{S1})$$

We work in the basis of J_z eigenstates under the labeling scheme presented in the main text. The J_z eigenstates for a spin- j system are denoted by $|j, m\rangle$, where

$$J_z |j, m\rangle = m |j, m\rangle. \quad (\text{S2})$$

The eigenstates of J_x , meanwhile, are denoted by $|j, m\rangle_x$, where

$$J_x |j, m\rangle_x = m |j, m\rangle_x. \quad (\text{S3})$$

These bases are related by a $\pi/2$ rotation about J_y : rewriting J_x as $e^{-i\frac{\pi}{2}J_y}J_z e^{i\frac{\pi}{2}J_y}$ we have

$$(e^{-i\frac{\pi}{2}J_y}J_z e^{i\frac{\pi}{2}J_y}) |j, m\rangle_x = m |j, m\rangle_x, \quad (\text{S4})$$

implying that

$$J_z (e^{i\frac{\pi}{2}J_y} |j, m\rangle_x) = m (e^{i\frac{\pi}{2}J_y} |j, m\rangle_x), \quad (\text{S5})$$

so we see that

$$|j, m\rangle_x = e^{-i\frac{\pi}{2}J_y} |j, m\rangle. \quad (\text{S6})$$

We define the parity operator used throughout the main text as

$$\Pi = e^{i\pi(J_z - j)}, \quad (\text{S7})$$

which has the properties $\Pi^2 = \mathbb{1}$ and $\Pi^\dagger = \Pi$. Because J_x^2 commutes with Π , they share a simultaneous eigenbasis, and we therefore seek the definite-parity eigenstates of J_x^2 . Noting that $\Pi J_x \Pi^\dagger = -J_x$, we have

$$\begin{aligned} \Pi J_x |j, m\rangle_x &= m\Pi |j, m\rangle_x \\ \Pi J_x (\Pi^\dagger \Pi) |j, m\rangle_x &= m\Pi |j, m\rangle_x \\ -J_x \Pi |j, m\rangle_x &= m\Pi |j, m\rangle_x, \end{aligned} \quad (\text{S8})$$

so we identify

$$\Pi |j, m\rangle_x = |j, -m\rangle_x. \quad (\text{S9})$$

The definite-parity eigenstates of J_x^2 thus have the form $\alpha |j, m\rangle_x + \beta |j, -m\rangle_x$. Substituting we find

$$\Pi(\alpha |j, m\rangle_x + \beta |j, -m\rangle_x) = \alpha |j, -m\rangle_x + \beta |j, m\rangle_x, \quad (\text{S10})$$

requiring $\alpha = \pm\beta$ (except when $m = 0$). We therefore define

$$|j, m\rangle_\pm = \frac{1}{\sqrt{2}}(|j, m\rangle_x \pm |j, -m\rangle_x) \quad (\text{S11})$$

when $m \neq 0$, and

$$|j, 0\rangle_+ = |j, 0\rangle_x. \quad (\text{S12})$$

It is clear, then, that

$$J_x^2 |j, m\rangle_\pm = m^2 |j, m\rangle_\pm \quad (\text{S13})$$

and

$$\Pi |j, m\rangle_\pm = \pm |j, m\rangle_\pm. \quad (\text{S14})$$

III. SEMICLASSICAL MODEL

In this section we summarize the semiclassical approach to modeling properties of the LMG Hamiltonian. We refer the reader to Refs. [5–8] for more thorough discussions of this approach and its applications.

A. Classical energy surface and ground state solutions

The semiclassical model discussed in the main text, and used below for the density of states calculation, is obtained by noticing that, in the thermodynamic limit, the angular momentum operators (J_x, J_y, J_z) can be replaced by a vector lying on a sphere of radius j :

$$(J_x, J_y, J_z) \leftrightarrow j(\sin \theta \cos \phi, \sin \theta \sin \phi, \cos \theta). \quad (\text{S15})$$

Substituting these into the LMG Hamiltonian we find

$$\mathcal{H}(\theta, \phi) = \frac{E(\theta, \phi)}{j} = -h \cos \theta - \frac{\gamma_x}{2} \sin^2 \theta \cos^2 \phi. \quad (\text{S16})$$

The same energy surface is also found by evaluating the expectation value of the Hamiltonian for a spin coherent state, $|\theta, \phi\rangle = e^{-i\phi J_z} e^{-i\theta J_y} |j, j\rangle$, in the limit $j \rightarrow \infty$. First, note that the taking the expectation value of each angular momentum operator gives

$$(\langle J_x \rangle, \langle J_y \rangle, \langle J_z \rangle) = j(\sin \theta \cos \phi, \sin \theta \sin \phi, \cos \theta). \quad (\text{S17})$$

For large j we have $\langle \theta, \phi | J_\alpha^2 | \theta, \phi \rangle \approx \langle \theta, \phi | J_\alpha | \theta, \phi \rangle^2$ where $\alpha = x, y, z$, and in the limit $j \rightarrow \infty$ the relation becomes exact. We therefore recover the energy surface given above,

$$\mathcal{H}(\theta, \phi) = \lim_{j \rightarrow \infty} \frac{1}{j} \langle \theta, \phi | H | \theta, \phi \rangle. \quad (\text{S18})$$

The ground states of the semiclassical model are found by differentiating \mathcal{H} with respect to θ and ϕ and setting the result equal to zero. Carrying out this calculation, one finds that when $h > \gamma_x$, there is a single minimum at $\theta_0 = 0$, with $E_{\min} = \mathcal{H}(0, \phi) = -h$. When $h < \gamma_x$, however, there are two distinct minima with $\phi_0 = 0, \pi$ and $\cos \theta_0 = \frac{h}{\gamma_x}$, with degenerate energies

$$E_{\min} = \mathcal{H}(\theta_0, 0) = \mathcal{H}(\theta_0, \pi) = -\frac{h^2 + \gamma_x^2}{2\gamma_x}. \quad (\text{S19})$$

We note that, for energy spectra plotted in the main text, we shift all energies such that the ground state energy is zero for all h/γ_x , which aids comparisons with the experimental results.

B. Density of states

In this section we present a calculation of the LMG density of states in the semiclassical approximation. The essential aspects of the calculation can be found in, e.g., Ref. [9]. Here we elucidate the details, as they provide valuable insights into the origin of the excited-state quantum phase transition and the connections between the quantum Hamiltonian and the semiclassical model.

For convenience, here we set $\gamma_x = 1$ and define $z = -\cos \theta$, so that the semiclassical Hamiltonian is given by

$$\mathcal{H}(z, \phi) = hz - \frac{1 - z^2}{2} \cos^2 \phi. \quad (\text{S20})$$

The density of states at an energy E is approximated semiclassically by the Gutzwiller trace formula:

$$\rho(E) = \frac{1}{4\pi} \int dz d\phi \delta[\mathcal{H}(z, \phi) - E]. \quad (\text{S21})$$

One can loosely imagine that this integral counts the number of points in the classical phase space with a given energy E . The normalization factor of 4π is obtained by integrating Eq. S21 over all values of E . We will approach this integral by first finding the z and ϕ which yield $\mathcal{H}(z, \phi) = E$ for a given E . It is helpful to note that, in the region $h \leq 1$, E is bounded from below by $E \geq -\frac{h^2+1}{2}$, while when $h \geq 1$, $E \geq -h$. In both cases, E is bounded from above by $E \leq h$.

For a given z and E , ϕ is determined by

$$\phi = \pm \cos^{-1} \left(\pm \sqrt{2 \frac{hz - E}{1 - z^2}} \right), \quad (\text{S22})$$

which only has solutions when

$$0 \leq 2 \frac{hz - E}{1 - z^2} \leq 1. \quad (\text{S23})$$

From this it is straightforward to show that, when $h \leq 1$,

$$-h - \sqrt{h^2 + 2E} \leq z \leq -h + \sqrt{h^2 + 2E}, \quad (\text{S24})$$

and when $h \geq 1$,

$$\frac{E}{h} \leq z \leq -h + \sqrt{h^2 + 2E}. \quad (\text{S25})$$

On the other hand, for a given ϕ and E , z takes one or both roots

$$z_{\pm} = \frac{-h \pm \sqrt{h^2 + \cos^2 \phi (2E + \cos^2 \phi)}}{\cos^2 \phi}. \quad (\text{S26})$$

First consider the case where $h \leq 1$. When $E < -h$, both values in Eq. S26 yield a valid $z \in [-1, 1]$. When $E > -h$, meanwhile, only the z_+ root is valid. This change is closely related to the excited state quantum phase transition: below the transition there are two distinct classical trajectories with the same E , while above, there is only one. This is depicted in Figure S2a, where we show curves of constant energy on top of the classical energy surface for $h = 0.18$. For energies below the transition, the constant-energy curves come in pairs. For $h \geq 1$, meanwhile, there is always only one valid solution, namely, the z_+ root.

To evaluate the integral in Eq. S21, we must also find the set of ϕ values for which there is at least one z such that $\mathcal{H}(z, \phi) = E$ for a given E . When $h \geq 1$, this is simply $\phi \in [0, 2\pi]$. We also have $\phi \in [0, 2\pi]$ for $h \leq 1$ when $E \geq -h$. The case where $h \leq 1$ and $E \leq -h$ is somewhat more complicated. Here ϕ takes values on two disjoint intervals:

$$\phi \in [-\phi_0, \phi_0] \quad (\text{S27})$$

and

$$\phi \in [\pi - \phi_0, \pi + \phi_0] \quad (\text{S28})$$

where in both cases

$$\phi_0 = \cos^{-1} \left(\sqrt{-h\zeta_-} \right) \quad (\text{S29})$$

and

$$\zeta_{\pm} = \frac{E}{h} \pm \sqrt{\left(\frac{E}{h} \right)^2 - 1} \quad (\text{S30})$$

(we will make use of ζ_+ shortly). In every case we denote the set of permissible ϕ values by Φ_E .

We now proceed with the integral in Eq. S21.

$$\rho(E) = \frac{1}{4\pi} \int_{\phi \in \Phi_E} d\phi \int_{-1}^1 dz \delta[g_{E,\phi}(z)] \quad (\text{S31})$$

where

$$g_{E,\phi}(z) \equiv \mathcal{H}(z, \phi) - E. \quad (\text{S32})$$

We apply the following property of the Dirac delta:

$$\int_{-\infty}^{\infty} dx f(x) \delta[g(x)] = \sum_i \frac{f(x_i)}{|g'(x_i)|} \quad (\text{S33})$$

where the x_i are the roots of $g(x)$. In our case the roots of $g(z)$ are the z_{\pm} we found above, and we have

$$g'(z_{\pm}) = \pm \sqrt{h^2 + \cos^2 \phi (2E + \cos^2 \phi)}. \quad (\text{S34})$$

We evaluate the integral in the following three regions: Region I, where $h \leq 1$ and $E \leq -h$; Region II, where $h \leq 1$ and $E \geq -h$; and Region III, where $h \geq 1$. Starting with Region I:

$$\rho_I(E) = \frac{1}{4\pi} \int_{-\phi_0}^{\phi_0} \frac{2 d\phi}{\sqrt{h^2 + \cos^2 \phi (2E + \cos^2 \phi)}} + \frac{1}{4\pi} \int_{\pi - \phi_0}^{\pi + \phi_0} \frac{2 d\phi}{\sqrt{h^2 + \cos^2 \phi (2E + \cos^2 \phi)}}, \quad (\text{S35})$$

which can be rewritten as

$$\rho_I(E) = \frac{2}{\pi} \int_0^{\phi_0} \frac{d\phi}{\sqrt{h^2 + \cos^2 \phi (2E + \cos^2 \phi)}}. \quad (\text{S36})$$

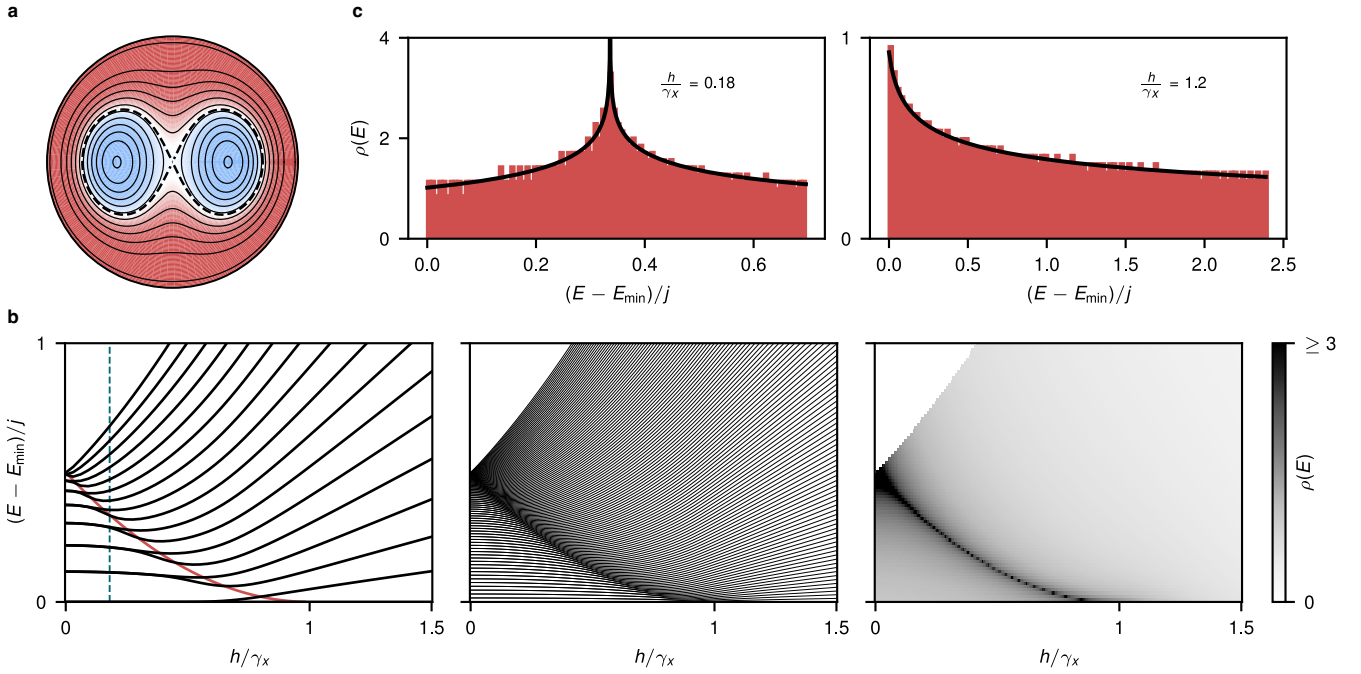


FIG. S2. Density of states of the LMG model. **a** The semiclassical energy surface $\mathcal{H}(\theta, \phi)$, represented in color, with constant-energy curves plotted on top. We use a polar projection of the sphere, where the radial coordinate is θ and the angular coordinate is ϕ ; in this mapping the north pole of the sphere corresponds to the center of the disk while the south pole corresponds to its boundary. **b** Energy spectra for $j = 8$ (left) and $j = 64$ (middle) and the semiclassical density of states (right). The red curve in the left panel is the critical energy of the ESQPT, and the vertical dashed line indicates the value of h/γ_x used in both the ESQPT experiments in the main text and in **a**. **c** Semiclassical density of states plotted on top of histograms of eigenenergies for $j = 500$.

We will evaluate this integral numerically, but we must first deal with the fact that the integrand has a singularity at $\phi = \phi_0$. Our approach will be to subtract a function from the integrand that has the same asymptotic behavior as $\phi \rightarrow \phi_0$, and that has an analytic solution, such that we can add its contribution back after the numerical integration. We first factor the denominator:

$$\rho_I(E) = \frac{2}{\pi} \int_0^{\phi_0} \frac{d\phi}{\sqrt{(\cos^2 \phi + h\zeta_+)(\cos^2 \phi + h\zeta_-)}}. \quad (\text{S37})$$

The origin of the singularity with $\phi = \phi_0 = \cos^{-1}(\sqrt{-h\zeta_-})$ is now clear. The function

$$\frac{1}{\sqrt{(\cos^2 \phi_0 + h\zeta_+)}} \frac{1}{\sqrt{(\cos^2 \phi + h\zeta_-)}} \equiv \frac{s(\zeta_+, \zeta_-)}{\sqrt{(\cos^2 \phi + h\zeta_-)}}, \quad (\text{S38})$$

where $s(\zeta_+, \zeta_-)$ is constant with respect to ϕ has the same asymptotic behavior as $\phi \rightarrow \phi_0$ as our integrand. Then

$$\rho_I(E) = \frac{2}{\pi} \int_0^{\phi_0} d\phi \left\{ \frac{1}{\sqrt{(\cos^2 \phi + h\zeta_+)(\cos^2 \phi + h\zeta_-)}} - \frac{s(\zeta_+, \zeta_-)}{\sqrt{(\cos^2 \phi + h\zeta_-)}} \right\} + \frac{2}{\pi} \int_0^{\phi_0} d\phi \frac{s(\zeta_+, \zeta_-)}{\sqrt{(\cos^2 \phi + h\zeta_-)}}. \quad (\text{S39})$$

The first integral is easily evaluated numerically, as we have in effect ‘subtracted away’ its singularity. The second integral, meanwhile, can be evaluated as

$$r(\zeta_+, \zeta_-) = \frac{2}{\pi} \int_0^{\phi_0} d\phi \frac{s(\zeta_+, \zeta_-)}{\sqrt{(\cos^2 \phi + h\zeta_-)}} = \frac{2}{\pi} s(\zeta_+, \zeta_-) \sqrt{\frac{1}{1 + h\zeta_-}} F\left(\phi_0, \frac{1}{1 + h\zeta_-}\right) \quad (\text{S40})$$

where $F(\phi, m)$ is the incomplete elliptic integral of the first kind. This contains a slight problem in that m here will generally be greater than 1, causing problems for the numerical evaluation of this expression. We can use the

following identity to rectify this problem:

$$F(\phi, m) = \frac{1}{\sqrt{m}} F \left(\sin^{-1}(\sqrt{m} \sin \phi), \frac{1}{m} \right). \quad (\text{S41})$$

Substituting $\phi = \phi_0$ and $m = \frac{1}{1+h\zeta_-}$ we obtain

$$F \left(\phi_0, \frac{1}{1+h\zeta_-} \right) = F \left(\frac{\pi}{2}, 1+h\zeta_- \right), \quad (\text{S42})$$

which is equal to the complete elliptic integral of the first kind, $K(1+h\zeta_-)$. Therefore,

$$r(\zeta_+, \zeta_-) = \frac{4}{\pi} s(\zeta_+, \zeta_-) K(1+h\zeta_-). \quad (\text{S43})$$

The density of states in Region I, then, is ultimately given by

$$\rho_I(E) = \frac{2}{\pi} \int_0^{\phi_0} d\phi \left\{ \frac{1}{\sqrt{(\cos^2 \phi + h\zeta_+)(\cos^2 \phi + h\zeta_-)}} - \frac{s(\zeta_+, \zeta_-)}{\sqrt{(\cos^2 \phi + h\zeta_-)}} \right\} + r(\zeta_+, \zeta_-), \quad (\text{S44})$$

where the integral is easily evaluated by standard numerical methods.

In Regions II and III the integrand is well-behaved, and noting that in both cases there is only one root of $g(z)$, the density of states is given by a numerical integral of

$$\rho_{\text{II}}(E) = \rho_{\text{III}}(E) = \frac{1}{4\pi} \int_0^{2\pi} \frac{d\phi}{\sqrt{h^2 + \cos^2 \phi (2E + \cos^2 \phi)}}. \quad (\text{S45})$$

In Figure S2b we show the energy spectrum for $j = 8$ (left) and $j = 64$ (middle), as well as the density of states as calculated here (right). The increased density of states near the critical energy is visible in the energy spectra, particularly for $j = 64$. This density diverges in the thermodynamic limit, and this divergence coincides with the splitting of even- and odd-parity pairs near the critical energy. Finally, in Figure S2c we quantitatively validate our calculation by plotting the semiclassical density of states for two values of h on top of a histogram of the respective eigenenergies for $j = 500$, obtained by numerical diagonalization.

[1] Koch, J. *et al.* Charge-insensitive qubit design derived from the Cooper pair box. *Physical Review A* **76**, 042319 (2007). URL <https://link.aps.org/doi/10.1103/PhysRevA.76.042319>.

[2] Blais, A., Grimsom, A. L., Girvin, S. & Wallraff, A. Circuit quantum electrodynamics. *Reviews of Modern Physics* **93**, 025005 (2021). URL <https://link.aps.org/doi/10.1103/RevModPhys.93.025005>.

[3] Wang, Z., Parker, R. W., Champion, E. & Blok, M. S. High-\$\{E\}\$-\$\{J\}\$-\$\{E\}\$-\$\{C\}\$ transmon qudits with up to 12 levels. *Physical Review Applied* **23**, 034046 (2025). URL <https://link.aps.org/doi/10.1103/PhysRevApplied.23.034046>. Publisher: American Physical Society.

[4] Champion, E., Wang, Z., Parker, R. W. & Blok, M. S. Efficient Control of a Transmon Qudit Using Effective Spin-\$\frac{7}{2}\$ Rotations. *Physical Review X* **15**, 021096 (2025). URL <https://link.aps.org/doi/10.1103/vbh4-lysv>. Publisher: American Physical Society.

[5] Leyvraz, F. & Heiss, W. D. Large-NScaling Behavior of the Lipkin-Meshkov-Glick Model. *Physical Review Letters* **95** (2005). URL <https://link.aps.org/doi/10.1103/PhysRevLett.95.050402>. Publisher: American Physical Society (APS).

[6] Castaños, O., López-Peña, R., Hirsch, J. G. & López-Moreno, E. Classical and quantum phase transitions in the Lipkin-Meshkov-Glick model. *Physical Review B* **74**, 104118 (2006). URL <https://link.aps.org/doi/10.1103/PhysRevB.74.104118>. Publisher: American Physical Society.

[7] Ribeiro, P., Vidal, J. & Mosseri, R. Exact spectrum of the Lipkin-Meshkov-Glick model in the thermodynamic limit and finite-size corrections. *Physical Review E* **78** (2008). URL <https://link.aps.org/doi/10.1103/PhysRevE.78.021106>. Publisher: American Physical Society (APS).

[8] Ribeiro, P., Vidal, J. & Mosseri, R. Thermodynamical Limit of the Lipkin-Meshkov-Glick Model. *Physical Review Letters* **99** (2007). URL <https://link.aps.org/doi/10.1103/PhysRevLett.99.050402>. Publisher: American Physical Society (APS).

[9] Nader, D. J., González-Rodríguez, C. A. & Lerma-Hernández, S. Avoided crossings and dynamical tunneling close to excited-state quantum phase transitions. *Physical Review E* **104** (2021). URL <https://link.aps.org/doi/10.1103/PhysRevE.104.064116>. Publisher: American Physical Society (APS).